The Seismic Record
A journal of the Seismological Society of America

Characterizing the Modes of Earth's Free Oscillations via Submarine Distributed Acoustic Sensing (DAS)

OPEN ACCESS

Balthazar Dubois-Dognon*[1], Chu-Fang Yang[1], and Anthony Sladen[1]

Abstract

Distributed acoustic sensing (DAS) on seafloor telecommunications cables is emerging as a powerful approach for observing geophysical processes. However, instrumental noise increases steeply below 10 millihertz (mHz), limiting the resolution of long-period signals. Here, we overcome this limitation by isolating low-frequency common-mode noise using channels with minimal signal amplitude, enabling the observation of low-frequency spectral peaks consistent with Earth's normal-mode oscillations in the mHz band along a submarine fiber-optic cable in the western Mediterranean Sea. Following the 2025 M_w 8.8 Kamchatka earthquake, we observe systematic variations in modal amplitudes with cable azimuth over 120 km, consistent with predictions from a normal-mode summation model. The amplitude is predicted above the noise level, but the signal is only observed after noise removal. This is explained by an event-independent response coefficient ($C \sim 0.13$), consistent with a flat instrumental response. Normal modes are also detected for smaller earthquakes down to M_w 7.7. The variably oriented cable resolves the radial and transverse horizontal components of motion. The large-scale signal's amplitude is locally modulated by variable cable azimuth, demonstrating a sensitivity for cable relocation. Our results demonstrate that DAS can resolve subtle solid-Earth deformation at mHz frequencies, opening new opportunities for large-scale, ocean-based monitoring of Earth structure and dynamics.

Cite this article as Dubois-Dognon, B., C.-F. Yang, and A. Sladen (2026). Characterizing the Modes of Earth's Free Oscillations via Submarine Distributed Acoustic Sensing (DAS), *The Seismic Record*. **6**(**3**), 358–367, doi: 10.1785/0320260014.

Supplemental Material

Introduction

Over the past decade, distributed acoustic sensing (DAS) has become a powerful means to probe sparsely instrumented regions such as submarine environments and ice sheets (e.g., Sladen *et al.*, 2019; Fichtner *et al.*, 2025). More recently, studies have explored its potential for low-frequency signals, including slow-slip events (e.g., tremors in the 2–10 Hz band by Baba *et al.*, 2023), iceberg calving in the 0.1–10 Hz range (Gräff *et al.*, 2025), and tsunami early warning down to 0.5–10 mHz (Becerril *et al.*, 2025). The latter shows from a laboratory experiment that the DAS strain noise floor rises as $1/f$: the response is not inherently less sensitive at low frequencies, but the elevated noise floor prevents reaching the high sensitivity typical near 0.1 s. This constitutes the main limitation for broader low-frequency applications. A key contributor is the so-called "common-mode" noise, which is caused by vibrations close to the interrogator, affecting all channels at the same time Ellmauthaler *et al.* (2017). This $1/f$ component, from laser phase noise, must be removed for low-frequency analyses. A straightforward approach averages signal-free channels to estimate and subtract the noise, with limitations discussed in the Data processing section. More advanced techniques have been proposed (e.g., Son *et al.*, 2025), but remain challenging to implement in practice, especially for normal modes which lack a clear wave train.

1. Université Côte d'Azur, CNRS, Observatoire de la Côte d'Azur, IRD, Géoazur, Valbonne, France, https://orcid.org/0009-0003-2434-3550 (BD-D); https://orcid.org/0000-0002-9595-7213 (C-FY); https://orcid.org/0000-0003-4126-0020 (AS)

*Corresponding author: balthazar.dubois@geoazur.unice.fr, balthazardub@gmail.com

One way to challenge the common-mode in DAS data is to investigate one of the most fundamental signals in low-frequency seismology: the free oscillations of the Earth. These oscillations can be modeled as a superposition of discrete normal modes linked to Earth structure. They are routinely observed after large earthquakes or through ambient noise data (Kobayashi and Nishida, 1998).

The modes were traditionally recorded by strain and pendulum seismographs (Benioff *et al.*, 1961). Submarine observations remain challenging because of sparse instrumentation and high horizontal noise, so ocean-bottom detections after large earthquakes rely mainly on the vertical component (Bécel *et al.*, 2011; Laske, 2021).

DAS interrogators send light pulses into a fiber-optic cable and collect the backscattered Rayleigh field along the optical path; the phase shift between two points is proportional to the longitudinal strain rate of that cable portion (Hartog, 2017). With a few meters of spatial resolution over tens of kilometers, the cable becomes a dense seismic array. However, its directional sensitivity and dependence on cable coupling complicate amplitude interpretation: a wave with displacement perpendicular to the cable produces zero net strain. The typical signal frequency range of the free oscillations of the Earth after a large earthquake is the mHz band. The broadband instrumental response of DAS is not fully characterized and may vary with local conditions (e.g., thermal stability), cable quality, or interrogator processing. Paitz *et al.* (2021) measured DAS strain-rate sensitivity over 17 octaves, indicating 10%–20% amplitude loss in the mHz band, whereas Lindsey *et al.* (2020) found a flat, near-identical response in the 1–120 s band.

In this study, we demonstrate the capability of DAS to observe the normal modes along a deep-seafloor telecom cable, where seismic data are otherwise costly, sparse, and temporary. We first demonstrate the observation of free oscillations of the Earth in the mHz band over a 120 km cable section located in the Ligurian Sea and following the 2025 M_w 8.8 Kamchatka earthquake. We analyze amplitude variations along the cable and compare them with a synthetic signal obtained from normal-mode summation. For the comparison, we use both a "true" model by computing the gradient of the velocity field, and test the approximation of a local apparent velocity to scale point-acceleration synthetics. In a second part, we investigate the ability of our approach to record normal modes following smaller magnitude events (M_w 7.7) and evaluate the retrieval of the modes' eigenfrequencies and attenuation. Finally, we show that a variably oriented DAS cable functions as a horizontal two-component strain meter, enabling discrimination between spheroidal and toroidal modes of oscillations needed for constraining the Earth's structure.

Detection of Free Oscillations of the Earth on DAS

We use the large M_w 8.8 earthquake that occurred in the Kamchatka peninsula on 29 July 2025 at 23:26:49 UTC, source parameters from the Global Centroid Moment Tensor (Global CMT) catalog: (Dziewonski *et al.*, 1981; Ekström *et al.*, 2012), latitude = 50.36° N, longitude = 158.23° E, depth = 36.3 km, half-time duration = 56.7 s, scalarmoment $= 1.58 \times 10^{29}$ dyn·cm). Data were recorded on a 160 km submarine telecom fiber-optic cable in the Ligurian Sea between Monaco and Italy (Fig. 1), which descends the continental slope (average 5° over the first 20 km), follows the slope base between 20 and 80 km optical distance, then climbs back up to Savona. The large magnitude allows clear observation over the first ~120 km; for smaller events the signal is detected to 70 km.

Modeling of the amplitude variation along the cable

To confront the observed low-frequency post-earthquake signature, we model the local strain rate $\dot{\varepsilon}_\phi(x,t)$ induced by a wave of incidence ϕ onto the cable as

$$\dot{\varepsilon}_\phi(x,t) = \frac{\partial}{\partial t}\frac{\partial}{\partial s} u_\phi(x,t) = \frac{\partial}{\partial t}(\mathbf{e}_\phi \cdot \nabla \mathbf{u}(x,t) \cdot \mathbf{e}_\phi), \tag{1a}$$

in which $\mathbf{u}(x,t)$ is the displacement vector field, $u_\phi(x,t)$ is its projection along the local cable direction $\mathbf{e}_\phi$, and $\frac{\partial}{\partial s}$ is the spatial derivative along the cable. Equation (1a) is the exact DAS strain rate: the cable orientation $\mathbf{e}_\phi(s)$ is time-invariant, so the time derivative commutes with the projection and, evaluated on the MINEOS velocity field $\mathbf{v} = \partial_t \mathbf{u}$, gives $\dot{\varepsilon}_\phi = \mathbf{e}_\phi \cdot \partial_s \mathbf{v}$ (a velocity gradient along the cable; the gradient method). For comparison, assuming an incident plane wave and a point measurement (gauge length $\ll$ wavelength):

$$\dot{\varepsilon}_\phi^{\mathrm{Syn}}(x,t) = \mathbf{e}_\phi \cdot \nabla\left(\frac{\partial u_\phi(x,t)}{\partial t}\right), \tag{1b}$$

$$= k_\theta v_\phi(x,t), \tag{1c}$$

$$= \frac{a_\phi(x,t)}{c_\theta}, \tag{1d}$$

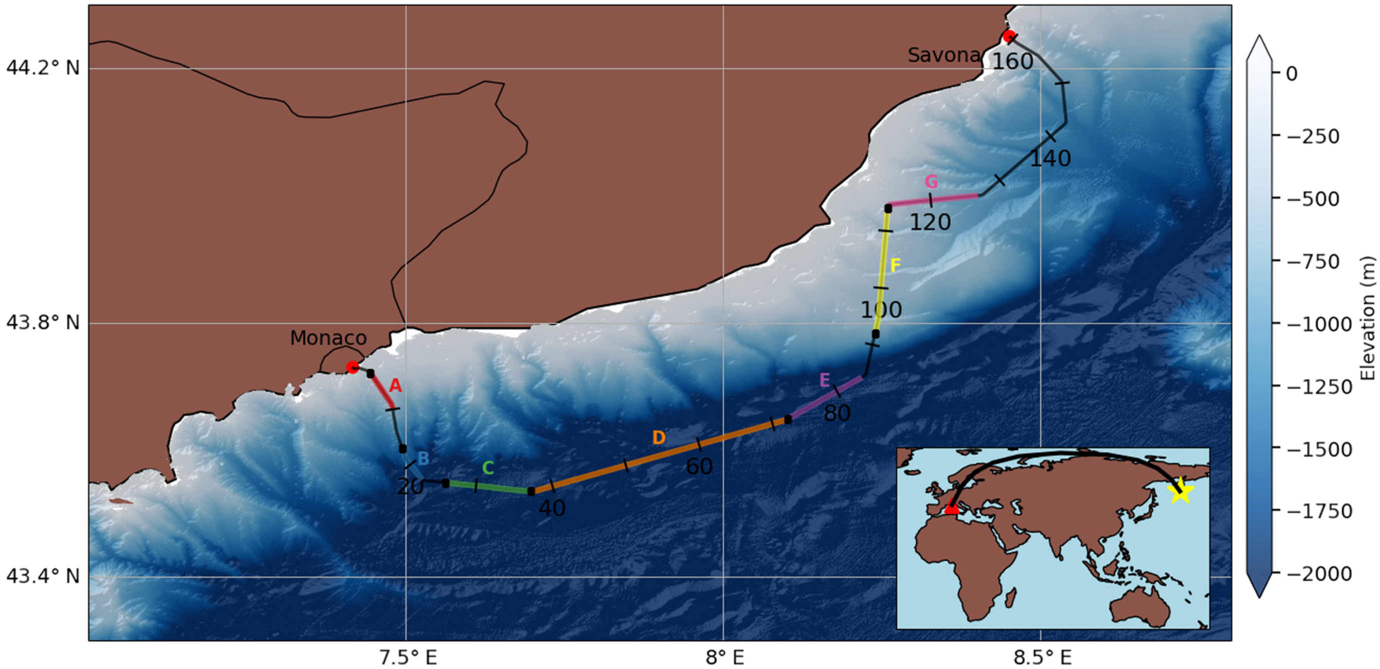

Figure 1. General setup of the study. Geometry of the dark fiber used in our study. The cable in laid in the Mediterranean Sea between Monaco and Savona, Italy. The localization of the channels is shown in black, and we separate them into constant azimuth sections colored and named from A to G. The source-receiver geometry for the 2025 M_w 8.8 Kamchatka earthquake is shown in the inset. The great circle path is emphasized as a black thick line. Inset: global source-station geometry.

in which $v_\phi(x,t)$ and $a_\phi(x,t)$ are velocity and acceleration along the cable, k_θ is the apparent wavenumber, and $c_\theta = c/\cos\theta$ the apparent phase velocity (c is the medium surface-wave phase velocity, ≈4.5 km s^{-1} in this frequency band), with $\theta = \phi - \phi^S$ the angle between the cable and the propagation direction (the source-station backazimuth). This point form a_ϕ/c_θ is the plane-wave (apparent-velocity) approximation of equation (1a): exact for a single plane wave, but unlike the gradient, it becomes singular near broadside ($\theta \to 90°$, $c_\theta \to \infty$). It nonetheless gives direct access to the cable's sensitivity to its own orientation and to source location. This formulation predicts azimuthal modulation of DAS amplitudes, which is tested against observations.

The strain-rate power spectral density is

$$P_{\dot{\varepsilon}}^{\text{Syn}}(x,\omega) \equiv A_{\text{Syn}}(\theta)^2 Y(\omega) \equiv A_{\text{Syn}}(x)^2 Y(\omega), \tag{2}$$

in which $A_{\text{Syn}}(\theta)$ encodes the source-cable geometry and $Y(\omega)$ the source spectral content. Using $\theta = \theta(x)$ along the cable, we denote this as $A(x)$ in the following sections.

Data processing

Raw phase-difference measurements are converted to strain rate, decimated to 1 Hz, detrended, and demeaned to construct a strain-rate time series. The gauge length is 20.42 m, and the data are binned along the cable in 100 m increments (~5 channels); channels within a bin are averaged to their mean value. A spatial low-pass filter (second-order Butterworth, cutoff wavelength 3 km) then reduces small-scale noise in the mHz band. Each binned channel is then Fourier transformed to obtain a power spectral density (PSD) as a function of frequency, computed per channel bin (i.e., per distance).

We model the data as low-frequency common-mode noise plus the normal-mode signal, whose amplitude is set by the source-cable geometry $A(x)$ of equation (1d), depending on the channel location x, whereas the noise affects all channels simultaneously. This is confirmed in Figure 2: raw PSD before (Fig. 2b) and during (Fig. 2c) the event is dominated by distance-constant energy lines (the common-mode noise) that exceed the signal we seek. Consequently, the measured data read:

$$d(x,t) = A(\theta(x))y(t) + n(t) \equiv A(x)y(t) + n(t). \tag{3}$$

Here, $y(t)$ is the source term common to all channels containing the frequency content of a specific moment tensor, $A(x) \equiv A(\theta(x))$ is the geometric amplitude response factor of the cable

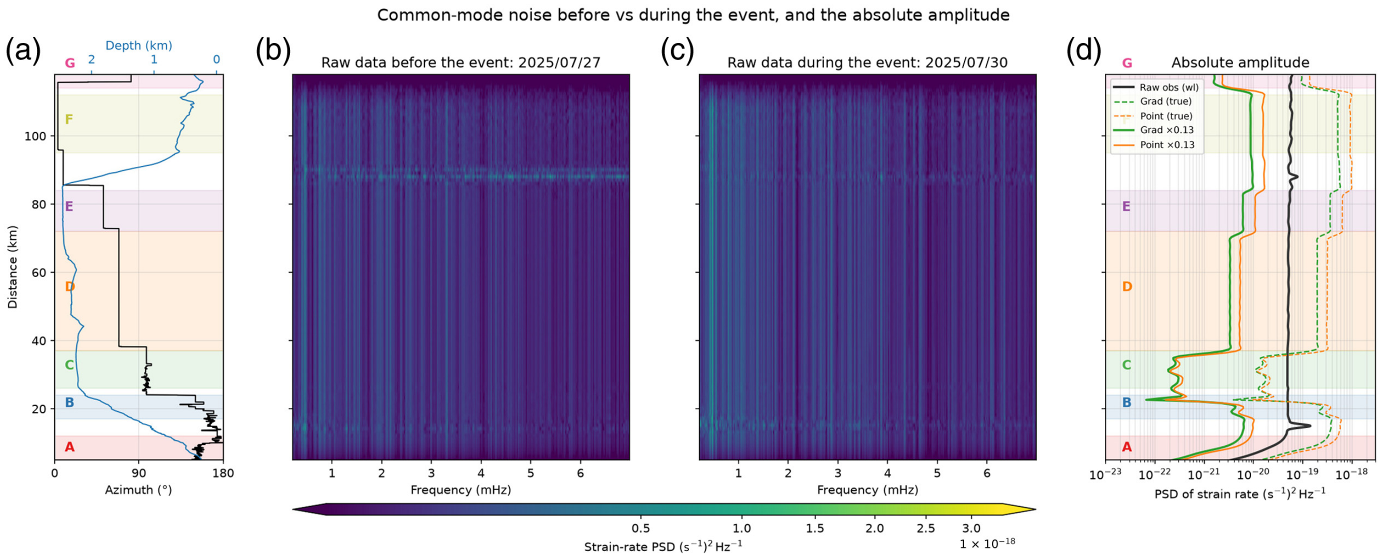

to the wave-field (equations 1a and 1d), $n(t)$ is the temporally coherent common-mode (instrument) noise—identical on every channel—and x_0 (introduced subsequently) is the reference channel. The equivalence is introduced because the cable azimuth varies with the optical distance x. For the rest of this text, the variable x will be preferred to θ because it is the standard variable used in DAS studies.

Figure 2d shows the raw amplitude profile $A(x)$ (common-mode noise), each distance bin being the mean power-spectral amplitude in the 2–6 mHz band, of order 0.2 nanostrain rate s^{-1}. The predicted amplitude (colors; gradient, equation 1a, and point, equation 1d) ranges from 0.1 (section C) to 100 (section F); the two differ because the point form is an approximation depending on c. The signal is thus expected above the noise in most sections, yet is not observed, motivating a frequency-flat response coefficient common to all channels:

$$A(x)y(t) \equiv A(x)y(t)C, \tag{4}$$

which explains the non-emergence of the signal above the noise level (a reduced amplitude relative to the expected signal), and is developed further subsequently.

The common-mode correction estimates $n(t)$ as the spatial mean of the raw channels over a reference window centered on x_0—a single $n(t)$ for the whole cable—and subtracts it from every channel. For long-wavelength normal modes, this removes absolute amplitudes, leaving only relative variations. Explicitly, with x_0 the reference channel, $\Delta s(x,x_0,t) = d(x,t) - d(x_0,t)$, which together with equation (2) gives

$$\Delta s(x,x_0,t) = [A(x) - A(x_0)]y(t), \tag{5}$$

Figure 2. (a) Typical power spectral density (PSD) of the common-mode noise recorded; (b) 3 days before the event in a quiet period; and (c) during the event. The noise energy is higher than the low-frequency signal excited by an M_w 8.8 earthquake, as the mode lines are not visible at this stage. (a): 120 km of the depth and azimuth profile of the Mediterranean Sea bottom cable. The noise signature is varying with time, which prevents a straightforward extraction before the event. Energy lines vary with frequency, but each is constant with respect to distance. This justifies our approach of common-mode mean removal in equation (5). (d) The black indicates millihertz (mHz) band averaged common-mode PSD amplitude, green- and orange-dashed indicates mean band PSD amplitude synthetics obtained from equations (1a) and (1d). The introduction of a constant response factor (C = 0.13) explains the non-observance of the signal above the noise level.

$\Delta s(x,x_0,t)$ cannot be directly compared to the absolute amplitude in equation (1d), but preserves evaluation of azimuthal sensitivity and validation of the model. Note that squaring Δs will contain cross products of $A(x)$ and $A(x_0)$, and we will later refer to the PSD of $\Delta s(x,x_0,t)$ as $\Delta S(x,x_0,\omega)$.

Considerations on the amplitude response of DAS to normal modes

On the expected absolute amplitude. Synthetic three-component accelerations are computed with MINEOS (Masters *et al.*, 2011) at virtual stations every half-kilometer along the cable. From these waveforms, we compute the exact along-cable strain rate $\mathbf{e}_\phi \cdot \partial_s \mathbf{v}$ (equation 1a) and the point apparent-velocity estimate (equation 1d), the latter projecting the acceleration onto the cable with phase velocity4.5 km s^{-1}, the spheroidal-mode average in this band. Both methodologies predict the same azimuthal variation.

The MINEOS acceleration spectrum (2–6 mHz) is consistent with nearby land seismic stations, supporting the forward model's validity (Fig. S1, available in the supplemental material to this article). Given the large wavelengths, similar amplitudes are expected offshore: in the preliminary reference Earth model (PREM) ocean model, fundamental modes spectral amplitudes at a sea-bottom seismometer are nearly identical with or without an ocean layer (Fig. S2a,b), ruling out order-of-magnitude ocean attenuation.

Observationally, an M_w 8.2 event (29 July 2021) recorded on an ocean-bottom seismometer (OBS) offshore Monaco, in a setting similar to ours, shows amplitudes that agree with on-land stations 50 km away (Fig. S2c,d).

Introduction of a constant response coefficient to explain the azimuthal amplitude variation along the cable. From the previous section, our modeling is validated against local seismic stations and an OBS, so the sea-bottom strain is well predicted. We next investigate the amplitude deficit by comparing the relative observed and synthetic amplitudes: subtracting the same reference channel x_0 from both makes them differential quantities, and any choice of x_0 recovers the same shape if the model is correct (Fig. S4).

To validate our modeling of relative amplitude variations, we fit the band-averaged PSD of difference, adapted from equations (2) and (5):

$$\Delta\hat{S}_{\mathrm{Obs}}(x,x_0) = \int_{\omega_0}^{\omega_1} \Delta S(x,x_0,\omega)d\omega, \tag{6}$$

with the band-averaged ($\omega_0 = 2$ mHz, $\omega_1 = 6$ mHz) synthetic relative strain rate PSD $\Delta\hat{S}_{\mathrm{Syn}}(x,x_0)$ by minimizing

$$\Phi(C) = \sum_{x,x_0}((\Delta\hat{S}^{\mathrm{Obs}})(x,x_0) - C(\Delta\hat{S}^{\mathrm{Syn}})(x,x_0))^2, \tag{7}$$

in which C is expected to be independent of x and x_0. It can thus be solved analytically by partial minimization, setting $\frac{\partial\Phi}{\partial C} = 0$:

$$C = \frac{\sum_{x,x_0=0}^{X} \Delta\hat{S}^{\mathrm{Obs}}(x,x_0)\Delta\hat{S}^{\mathrm{Syn}}(x,x_0)}{\sum_{x=0}^{X}(\Delta\hat{S}^{\mathrm{Syn}}(x,x_0))^2}. \tag{8}$$

We compute C by sweeping the reference channel x_0 over 2 km bins and obtain a constant value of $C(x_0) \equiv C \equiv 0.13$. This corresponds to a factor of 7.7 amplitude reduction.

The depth profile and along-cable azimuth are shown in Figure 3a. This geometry provides a wide range of orientations, leading to the observed amplitude variability (Fig. 3b,c). Clear mode lines can be identified in Figure 3b. Frequency-independent energy peaks are observed at the end of sections A and E. Although we do not explain the former, the latter is the result of vortex-induced vibrations (VIV; Mata Flores *et al.*, 2023). For each station, we use the mean amplitude in the 2–6 mHz band over a 20-hr window following the earthquake. The response coefficient C closely matches the observations (Fig. 3c); a direct comparison of the section-wise stacked spectra with the synthetic (Fig. S3) confirms a good fit of the predicted mode excitation for this event.

Results show strong azimuthal dependence controlled by cable orientation, with additional correlations to bathymetry (in the abyssal plain, between 40 and 80 km) highlighting DAS sensitivity to small-scale amplitude variations. We next assess detectability and azimuthal sensitivity for a larger set of events.

Detection for smaller earthquakes and implications for azimuthal sensitivity

We assess our processing on smaller events using the Global CMT catalog. First, we consider an M_w 7.9 aftershock of the M_w 8.8 Kamchatka earthquake (18 September 2025). Given the similar source location and propagation path, comparable amplitude variations are expected. The reference channel is kept the same, in section C.

An M_w 7.7 earthquake in the Drake Passage (Fig. 4e–h), despite its different location, has a similar θ profile along the cable (Fig. 4c,g) and is recovered with a minimum-amplitude reference channel in section C; normal modes appear over more than 70 km thanks to favorable geometry (high apparent-velocity amplification). Smaller-event amplitudes are thus recoverable when excitation is favorable. These signals are absent in the 24 hr before the event and emerge near the Global CMT origin time (Fig. S5), supporting their seismic origin.

For both events, we stacked the spectra in section D to increase the signal-to-noise ratio (SNR) and computed the cross spectra with the synthetics; both yield a correlation score ≥0.6 in the 1.5–4 mHz band, with good agreement of the lower frequency modes (Fig. S6).

The geometric sensitivity follows from projecting the ground motion onto the cable: a spheroidal (radial, Rayleigh-type) mode produces an axial strain $\propto \cos^2\theta$, whereas a toroidal (transverse, Love-type) mode produces $\propto \frac{1}{2}\sin 2\theta = \sin\theta\cos\theta$ (peaking at 45°). Both vanish at $\theta = 90°$ (cable perpendicular to propagation) where the apparent velocity c_θ diverges (Martin *et al.*,

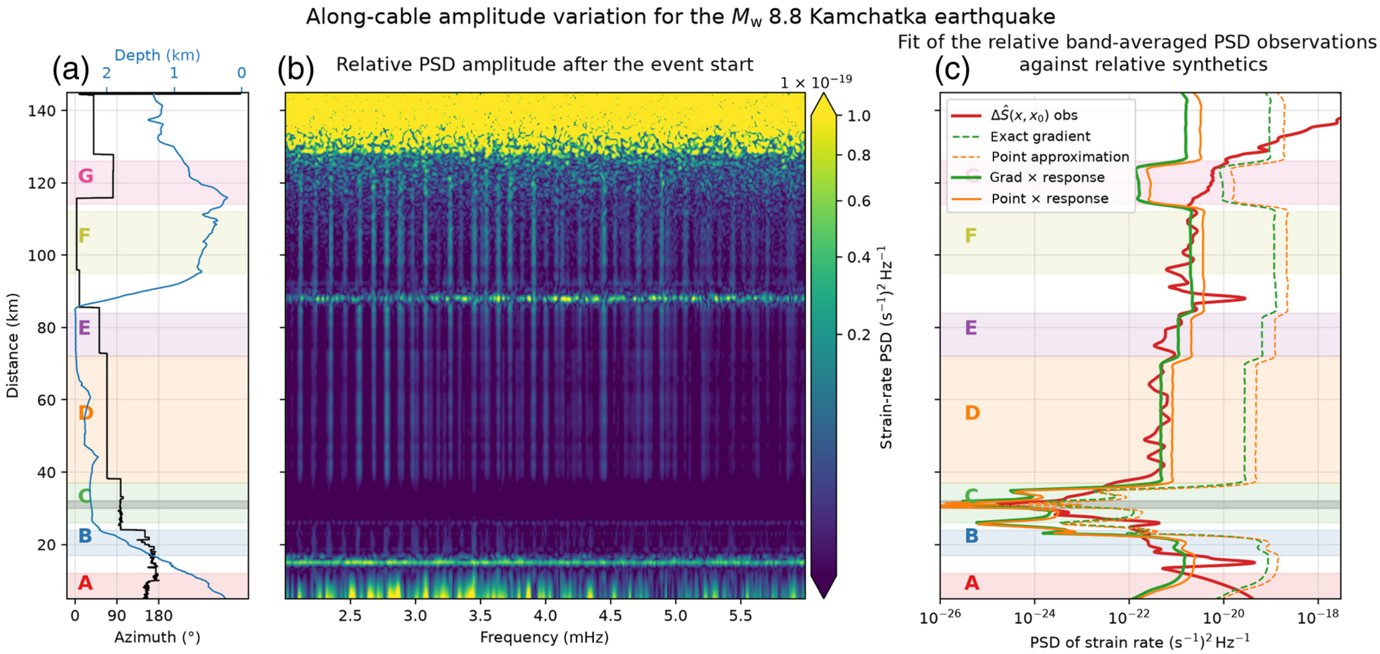

Figure 3. Variation of the normal-mode amplitude along cable distance and azimuth. (a) Along-track cable depth (blue) and azimuth (black). The seven good signal-to-noise ratio (SNR) constant azimuth cable sections A–G are outlined with different colors. (b) PSD of strain rate at each channel along the cable path. Clear vertical yellow lines show the normal modes of the Earth in the mHz band. (c) Mean observed relative amplitude in the 2–6 mHz band (red) and synthetic relative amplitude based on a MINEOS normal-mode simulation (green). The dashed lines represent the original relative amplitude that is reduced using a response factor C = 0.13. The common mode was removed inside section C for both. The synthetic curve is shifted by the factor a in equation (7) to match the relative amplitude profile, because the absolute amplitude is lost during the common-mode removal (see the Data processing section).

2021). Figure S7 shows these curves while indicating where each cable section stands for the events analyzed here (Fig. S7a), and illustrates how an azimuthally distributed catalog would sample the full sensitivity range (Fig. S7b,c).

The events recorded here have azimuths similar to the Kamchatka backazimuth and so sample a narrow range of θ, but next-generation DAS interrogators capable of detecting global oscillations of smaller amplitude, excited from more and better-distributed events would make such a geometric calibration practical.

Characterizing the Separation of Modes and the Attenuation Factor

Although absolute amplitudes cannot be recovered, DAS data still allow estimation of eigenfrequencies and mode attenuation, both sensitive to Earth structure. The high spatial sampling (20.42 m gauge length; ~6000 channels over 120 km) improves spectral SNR. Because the smaller events show a distance-dependent SNR reduction, we focus the detailed analysis on the M_w 8.8 Kamchatka mainshock.

Modes of oscillation

In the normal-mode framework, horizontal deformation results from spheroidal (radial, *SV*-like) and toroidal (transverse, *SH*-like) modes. Ellipticity and rotation couple fundamental modes through the Coriolis force, whereas overtones remain largely uncoupled (e.g., Schneider, 2022). Unlike a seismometer, the fiber cannot be rotated into an RT coordinate system; it records a projection of the wavefield onto its local orientation, usually a composite of radial and transverse components.

Stacked spectra from cable segments of varying azimuth reveal orientations from transverse to radial (red-to-blue colored curves, Fig. 5a). Clear separation is observed in two sections (toroidal in section C:26–37 km and radial in section F:95–112 km), with mixed components elsewhere. The peaks associated with the fundamental modes sometimes indicate a clear spheroidal mode (e.g., ${}_0S_{19}$), or a separation between toroidal and spheroidal if the frequencies are well separated from one another (e.g., ${}_0[S_{15}, T_{16}]$ in the zoom-in panels).

Recording of mode attenuation

Averaging along azimuthal sections reveals spatially variable attenuation (Fig. 5b–e), mainly controlled by local amplitude variations. For example, section D (37–72 km) attenuates faster

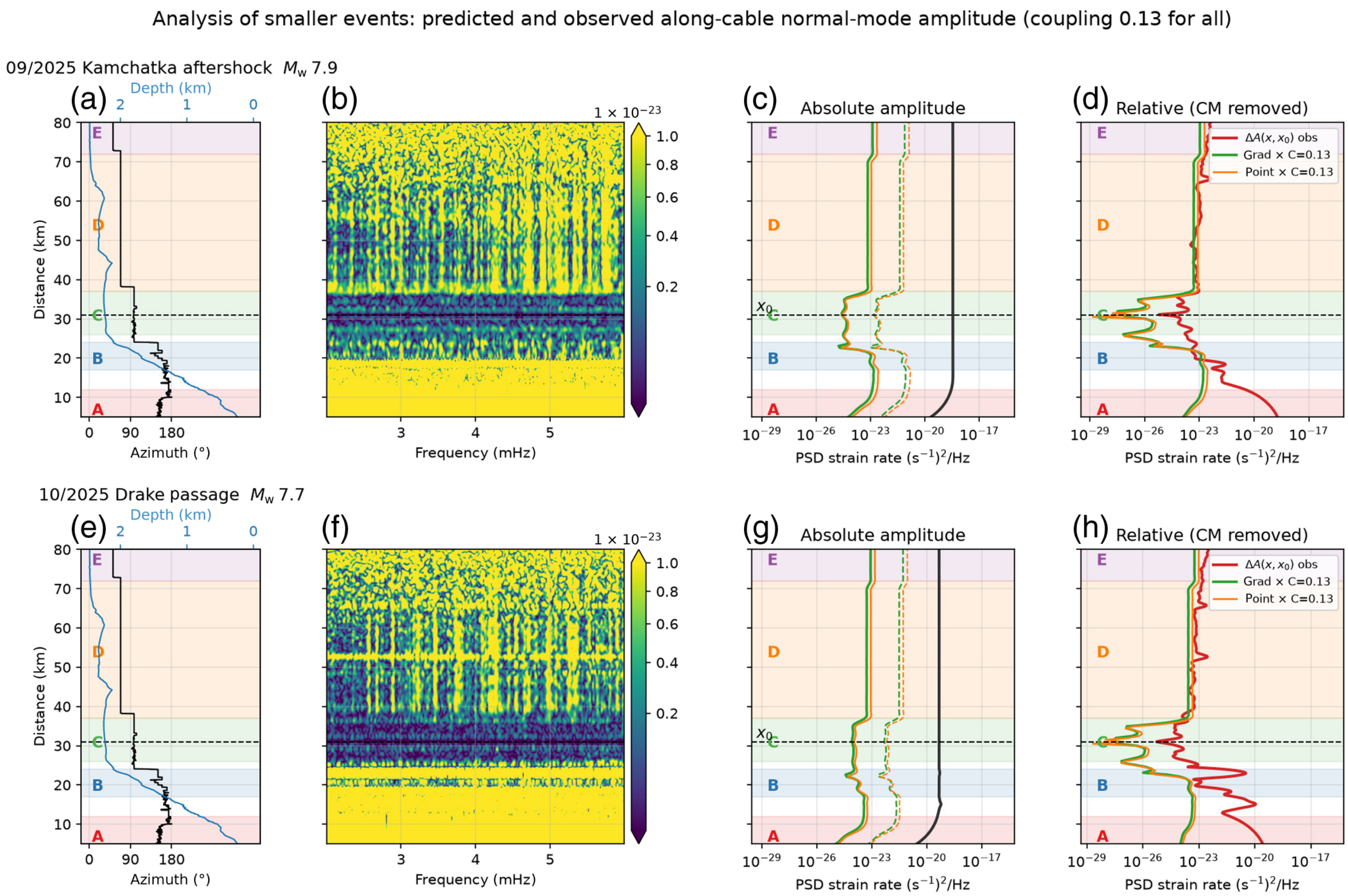

than section C (26–37 km). This occurs because the cable orientation results in a lower initial amplitude, causing the signal to drop more rapidly below the noise floor. All sections show exponential decay, with lower frequencies attenuating more slowly.

Using PREM eigenfrequencies, we estimate modal attenuation by fitting exponential decays to fundamental modes between 2 and 5 mHz (see Text S1); the fit is performed mode-by-mode in a narrow window around each PREM eigenfrequency. Example fits are shown in Figure 5f–i. The stacked spectrum of each constant-azimuth section (A–F) is fitted, and the reported Q is the mean over those sections, with uncertainty from their deviation. The mean values agree well with PREM (second value): ${}_0S_{19}$ (249 versus 250), ${}_0S_{24}$ (226 versus 212), ${}_0T_{24}$ (122 versus 138), and ${}_0S_{35}$ (120 versus 130). Across all fitted modes (Tables S1 and S2), the agreement is more variable; spheroidal modes are generally well constrained, whereas toroidal modes are more reliably measured between 2.8 and 4.5 mHz. This likely reflects lower signal amplitudes at lower frequencies (Fig. 5b–e), due to weaker excitation and/or reduced SNR. A complete summary of fitted fundamental modes (Tables S1 and S2) is illustrated in Figure S8.

Figure 4. Same as Figure 3 for an M_w 7.9 event that occurred in the Kamchatka peninsula 2.5 months after the larger event, in September 2025 (panels a–d); panels (e–h) show the M_w 7.7 Drake Passage event of 10 October 2025. (c) and (g) show the absolute amplitude of the synthetics (colored) and the high amplitude raw data (black). (d) and (h) show the common-mode corrected synthetics and data as in Figure 3c. A different channel in the long section D ($x_0 = 47$ km) is used as the reference section for subtracting the common-mode noise. The amplitude in section D is not recovered because the SNR is too low, with the amplitude trend dominated by the instrumental noise.

Discussions and Concluding Remarks

Across several major earthquakes (M_w 7.7 to 8.8), we observed the azimuthal variation of normal-mode signals along 120 km of DAS cable offshore Monaco. The modal signals were retrieved with a plane-wave point approximation, but the absolute amplitude was compromised by the pervasive low-frequency common-mode noise typical of DAS interrogators. During the largest event, the common-mode noise is of $n(x) \sim 0.1$ nanostrain.s^{-1}, comparable to or below the predicted amplitude depending on the local $A^{\mathrm{Syn}}(x)$, suggesting reduced sensitivity to long-period signals. Beyond the spectral

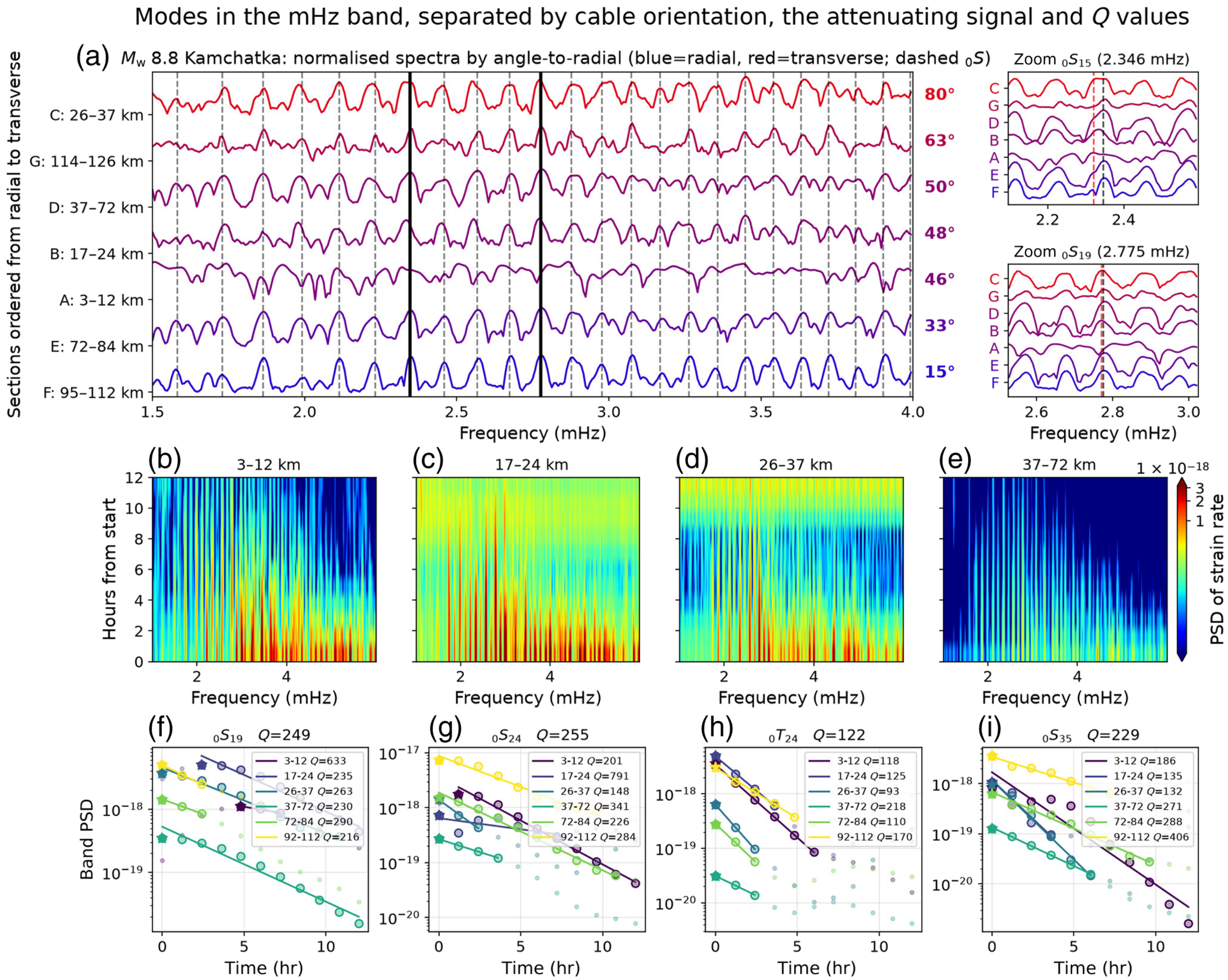

peaks themselves, the seismic origin of the signal is supported by its agreement with the normal-mode synthetic and by the recurrence of the same modes across the independent events analyzed here, section-D stacked spectra for which correlate well with the synthetics (Fig. S6).

Subtracting a reference section turns the DAS measurements into differential quantities, which we model to recover the azimuthal amplitude variations for events around the globe. The minimum magnitude for unequivocal detection is M_w 7.7. Lower magnitudes can probably be achieved with a better knowledge of the common-mode noise or using advanced noise-separation techniques.

The corrected DAS spectra yield spectral peaks and attenuation estimates consistent with PREM, and the variable cable orientation separates radial and transverse components, enabling identification of spheroidal and toroidal modes.

Figure 5. Characterization of the normal mode after the M_w 8.8 Kamchatka earthquake. (a) Normal mode of the Earth recorded on distributed acoustic sensing (DAS) and separated by channel bins of constant azimuth (A–G). A blue line indicates a strain direction in the radial direction (with respect to the source located in the Kamchatka peninsula), and a red line corresponds to the transverse direction. The angle to the radial direction is indicated on the right side of the panel next to each spectrum. Zoom-in panels point out the attention on modes ${}_0[S_{15},T_{16}]$ and ${}_0[S_{19},T_{20}]$ which illustrate the separation of toroidal and spheroidal modes. The black dashed line indicates the panel-specific spheroidal mode and the red dashed line indicates the $l+1$ toroidal mode. (b–e) Time evolution of the amplitude in the mHz band. The time in hours indicates an eight-hour-segment start time (relative to the event start time). The segments overlap by 80%.

The high spatial density of DAS enables efficient stacking and the retrieval of horizontal modes even in noisy submarine environments, which, to our knowledge, has not been demonstrated before; Coriolis-coupled toroidal modes have so far been observed only on the vertical component (e.g., Laske, 2021). The agreement with PREM and the limited variability (~20%) are comparable with the uncertainties of global normal-mode attenuation studies that rely on large datasets and inverse modeling (Talavera-Soza *et al.*, 2025), whereas our estimates come from a single large event on one submarine cable. Although this does not yet provide independent constraints on Earth structure, it shows that DAS measurements are consistent with state-of-the-art attenuation models and could contribute to future inversions.

The observed strain rate matches the normal-mode prediction up to a single multiplicative response factor, identical for every event analyzed (~0.13 in amplitude). Such an event-independent factor is the signature of a flat, instrument-response-like transfer loss rather than an unmodeled geophysical effect.

Our results add low-frequency seismology as a further motivation for DAS deployments, including in extraterrestrial contexts. Previous work highlighted DAS for dense-array seismology with reduced logistics and cost, mainly for subsurface imaging and ballistic waves on short (few kilometers) cables (Harmon *et al.*, 2024; Zhai *et al.*, 2024); separating radial and toroidal components instead requires longer, variably oriented cables.

Data and Resources

The raw 1 s data and the figure-reproduction code are at the Zenodo repository at doi: 10.5281/zenodo.19349504, including daily data before and during the 29 July Kamchatka mainshock and 12 hr for the September aftershock and Drake Passage event (netCDF format). Data processing was performed using the Xdas Python library (Trabattoni *et al.*, 2025). The supplemental material includes Text S1, Figures S1–S8, and Tables S1 and S2. The spatially downsampled 100 Hz dataset (six stations every 5 km and 0–30 km) is available under network code FF (Sladen *et al.*, 2025).

Declaration of Competing Interests

The authors acknowledge that there are no conflicts of interest recorded.

Acknowledgments

The distributed acoustic sensing acquisition was made possible thanks to the MARMOR project (ANR-21-ESRE-0020, France 2030) and access to the cable provided by Monaco Telecom. B. D-D. was funded by the MARMOR project and EPOS France, and C-F. Yang by the D-LIGHT project under Grant ANR-24-RRII-0001. The authors thank the technical team of Alcatel Submarine Networks for their support in the operation of the optoDAS interrogator, and the engineers at the Côte d'Azur observatory for maintaining the on-land seismic network used in this study. The first author thanks Martijn van den Ende for numerous discussions.

References

Baba, S., E. Araki, Y. Yamamoto, T. Hori, G. Fujie, Y. Nakamura, T. Yokobiki, and H. Matsumoto (2023). Observation of shallow slow earthquakes by distributed acoustic sensing using offshore fiber-optic cable in the Nankai trough, Southwest Japan, *Geophys. Res. Lett.* **50,** no. 12, doi: 10.1029/2022GL102678.

Bécel, A., M. Laigle, J. Diaz, J.-P. Montagner, and A. Hirn (2011). Earth's free oscillations recorded by free-fall OBS ocean-bottom seismometers at the lesser Antilles subduction zone, *Geophys. Res. Lett.* **38,** no. 24, doi: 10.1029/2011GL049533.

Becerril, C., A. Sladen, J. Ampuero, J. Preciado-Garbayo, M. González-Herráez, F. Kutschera, A. Gabriel, and F. Bouchette (2025). Towards tsunami early-warning with distributed acoustic sensing: Expected seafloor strains induced by tsunamis, *ESS Open Archives*, doi: 10.22541/essoar.174982683.32448422/v1.

Benioff, H., F. Press, and S. Smith (1961). Excitation of the free oscillations of the earth by the Chilean earthquake of May 22, 1960, *J. Geophys. Res.* **66,** no. 2, 605–619, doi: 10.1029/JZ066i002p00605.

Dziewonski, A. M., T.-A. Chou, and J. H. Woodhouse (1981). Determination of earthquake source parameters from waveform data for studies of global and regional seismicity, *J. Geophys. Res.* **86,** no. B4, 2825–2852, doi: 10.1029/JB086iB04p02825.

Ekström, G., M. Nettles, and A. M. Dziewoński (2012). The global CMT project 2004–2010: Centroid-moment tensors for 13,017 earthquakes, *Phys. Earth Planet. In.* **200-201,** 1–9, doi: 10.1016/j.pepi.2012.04.002.

Ellmauthaler, A., M. Willis, X. Wu, and M. LeBlanc (2017). Noise sources in fiber-optic distributed acoustic sensing VSP data, *79th EAGE Conference and Exhibition 2017*, European Association of Geoscientists and Engineers, Vol. 2017, 1–5.

Fichtner, A., F. Walter, A. Brisbourne, A. D. Booth, J. M. Kendall, T. Hudson, P. Paitz, and B. P. Lipovsky (2025). Fibre-optic exploration of the cryosphere, *Geophys. J. Int.* **244,** no. 2, ggaf489, doi: 10.1093/gji/ggaf489.

Gräff, D., B.P. Lipovsky, A. Vieli, A. Dachauer, R. Jackson, D. Farinotti, J. Schmale, J.P. Ampuero, E. Berg, A. Dannowski, *et al.* (2025). Calving-driven fjord dynamics resolved by seafloor fibre sensing, *Nature* **644,** no. 8076, 404–412, doi: 10.1038/s41586-025-09347-7.

Harmon, N., R. Porter, C. Rychert, N. Schmerr, M. M. Smith, Z. Shen, W. Wu, J. Giles, N. McCall, J. Wang, *et al.* (2024). Distributed acoustic sensing for future planetary applications: Initial results from the San Francisco volcanic field, a Lunar analogue, *Earth Space Sci.* **11,** no. 12, e2024EA003640, doi: 10.1029/2024EA003640.

Hartog, A. H. (2017). *An Introduction to Distributed Optical Fibre Sensors*, First Ed., CRC Press, Boca Raton, Florida.

Kobayashi, N., and K. Nishida (1998). Continuous excitation of planetary free oscillations by atmospheric disturbances, *Nature* **395,** no. 6700, 357–360, doi: 10.1038/26427.

Laske, G. (2021). Observations of earth's normal modes on broadband ocean bottom seismometers, *Front. Earth Sci.* **9,** 679958, doi: 10.3389/feart.2021.679958.

Lindsey, N. J., H. Rademacher, and J. B. Ajo-Franklin (2020). On the broadband instrument response of fiber-optic DAS Arrays, *J. Geophys. Res. Solid Earth* **125,** no. 2, e2019JB018145, doi: 10.1029/2019JB018145.

Martin, E. R., N. J. Lindsey, J. B. Ajo-Franklin, and B. L. Biondi (2021). Introduction to interferometry of fiber-optic strain measurements, in *Distributed Acoustic Sensing in Geophysics*, Chapter 9, Y. Li, M. Karrenbach, and J. B. Ajo-Franklin (Editors), American Geophysical Union (AGU), Washington, D.C., 111–129.

Masters, G., J. H. Woodhouse, and G. Freeman (2011). MINEOS v1.0.2. Software.

Mata Flores, D., A. Sladen, J.-P. Ampuero, E. D. Mercerat, and D. Rivet (2023). Monitoring deep sea currents with seafloor distributed acoustic sensing, *Earth Space Sci.* **10,** e2022EA002723, doi: 10.1029/2022EA002723.

Paitz, P., P. Edme, D. Gräff, F. Walter, J. Doetsch, A. Chalari, C. Schmelzbach, and A. Fichtner (2021). Empirical investigations of the instrument response for distributed acoustic sensing (DAS) across 17 octaves, *Bull. Seismol. Soc. Am.* **111,** no. 1, 1–10, doi: 10.1785/0120200185.

Schneider, S. A. (2022). Toroidal mode observations and their interpretation in terms of anisotropy and density, *Ph. D. Thesis*, Utrecht University, Utrecht, The Netherlands.

Sladen, A., B. Dubois-Dognon, and , and Epos-France (2025). FF: French fiber network, available at https://www.fdsn.org/networks/detail/FF/ (last accessed April 2026).

Sladen, A., D. Rivet, J. P. Ampuero, L. De Barros, Y. Hello, G. Calbris, and P. Lamare (2019). Distributed sensing of earthquakes and ocean-solid Earth interactions on seafloor telecom cables, *Nat. Commun.* **10,** no. 1, 5777, doi: 10.1038/s41467-019-13793-z.

Son, Y., B. Yoon, K. Hong, M.-H. Lee, J. Lee, and S.-J. Choi (2025). Common-mode noise separation in distributed acoustic sensing vertical seismic profile data: A self-supervised deep learning approach with enhanced blind network, *J. Appl. Geophys.* **233,** 105634, doi: 10.1016/j.jappgeo.2025.105634.

Talavera-Soza, S., L. Cobden, U. H. Faul, and A. Deuss (2025). Global 3D model of mantle attenuation using seismic normal modes, *Nature* **637,** no. 8048, 1131–1135, doi: 10.1038/s41586-024-08322-y.

Trabattoni, A., M. Baillet, M. V. D. Ende, D. Rivet, E. Stutzman, C. Strumia, and F. Biagioli (2025). Xdas: A python framework for distributed acoustic sensing, *Seismol. Res. Lett.* **96,** no. 5, 3221–3230.

Zhai, Q., A. Husker, Z. Zhan, E. Biondi, J. Yin, F. Civilini, and L. Costa (2024). Assessing the feasibility of distributed acoustic sensing (DAS) for moonquake detection, *Earth Planet. Sci. Lett.* **635,** 118695, doi: 10.1016/j.epsl.2024.118695.

Manuscript received 10 April 2026
Published online 2 September 2026